# Substrate optimization with the adjoint method and layered medium Green's functions

Ergun Simsek,* Raonaqul Islam, Sumya H. Oishe, and Curtis R. Menyuk

*Department of Computer Science and Electrical Engineering, University of Maryland Baltimore County, Baltimore, Maryland 21250, USA*
*\*simsek@umbc.edu*

In recent years, the photonics community has shown increasing interest in the inverse design of photonic components and devices using the adjoint method (AM) due to its efficient gradient computation and suitability for large parameter and continuous design spaces. This work focuses on substrate optimization to maximize light transmission or field enhancement at specific locations using layered medium Green's functions (LMGFs). We first provide a numerical formulation for calculating two-dimensional (2D) LMGFs, leveraging their efficiency for fixed sources and observation points parallel to layer interfaces. We then present a step-by-step implementation of the AM for substrate optimization using LMGFs. Through numerical studies, we verify the field enhancement achieved with AM-designed substrates using a frequency-domain solver. We compare the results of AM with particle swarm optimization (PSO) for two optimization problems, demonstrating that AM not only generates realistic designs with smooth permittivity profiles but also achieves inverse design more efficiently than PSO. The AM designs are easier to fabricate and require significantly less computational effort due to the efficient gradient computation inherent in the method. This study underscores the advantages of AM in designing photonic devices with continuous parameter spaces.     © 2024 Optica Publishing Group. All rights, including for text and data mining (TDM), Artificial Intelligence (AI) training, and similar technologies, are reserved.

## 1. INTRODUCTION

In the last decade, there has been growing interest in the photonics community in the inverse design of photonic components and devices using the adjoint method (AM) [1–13]. This choice has several advantages over other modern numerical optimization techniques, such as particle swarm optimization (PSO) [10,14–16] and the genetic algorithm (GA) [10,14,17]. First, AM provides efficient computation of gradients with respect to design parameters with a computational cost that is independent of the number of design parameters. This unique property of AM is particularly advantageous in optimization problems where the number of design parameters is large. Second, AM is well suited for problems with continuous design spaces, where the design parameters can take on any real value within user-determined limits. GA and PSO, on the other hand, face challenges in handling continuous design spaces, especially if the number of parameters to be optimized is large, e.g., as the number of parameters increases in a PSO implementation, the search space expands exponentially, making it harder for the swarm to explore effectively and find optimal solutions. This leads to sparse sampling and slower convergence since particles take longer to locate promising regions. Additionally, the risk of premature convergence to sub-optimal solutions rises, complicating the optimization process. The fitness landscape in

high-dimensional spaces is more complex, with numerous local optima and steep gradients, making navigation through this space and global optimization difficult.

Substrate optimization for maximizing the transmission of light through the substrate or maximizing the field at a specific location at a desired wavelength or wavelength range typically involves designing the properties of the substrate material, such as the permittivity and thickness [11–13,18–26]. It is known that stacks of thin films with varying refractive indices and coatings with a gradually changing refractive index can reduce reflections, and AM has already been utilized to design substrates [11,12]. In those studies [11,12], researchers have used either the frequency-domain finite differences (FDFD), time-domain finite differences (FDTD), or the transfer-matrix method. Here, we achieve the same goal using layered medium Green's functions (LMGFs).

For a multi-layered planar geometry, LMGFs give us the electric and magnetic fields created by electrical or magnetic dipoles or line sources placed at any location in that multi-layered geometry [27–30]. As discussed later, the LMGF formulation requires less computation time for the solution if the computation makes use of the following fact: for a fixed source, if the coordinates of observation points change parallel to the layer interfaces, then one needs to calculate the spectral

domain LMGFs only once, and their spatial counterparts can be computed via adaptive integration all at once.

The outline of this paper is as follows. We first provide a complete formulation to calculate the two-dimensional (2D) LMGFs numerically. Then we provide a step-by-step recipe to implement an adjoint method for substrate optimization using LMGFs. In the numerical results section, we verify the field enhancement that is achieved with substrates that are designed with the adjoint method using a frequency-domain finite-differences (FDFD) solver for two different optimization problems and conclude.

## 2. EVALUATION OF 2D LMGFs

Previously, we followed the formulation developed by Chew [27] to calculate the LMGFs for line [28] and dipole [29] sources. Both studies reduced computation time by subtracting the singularities from the spectral domain LMGFs and adding their contributions to the spatial domain using some Bessel and Hankel function formulae. Here, we follow the recursive formulation developed initially for anisotropic medium LMGFs [30] as follows.

Figure 1 illustrates a medium with $N+1$ layers aligned parallel to the $x$-axis, where each layer is defined with its electrical permittivity ($\epsilon_\ell = \epsilon_0 \epsilon_{r,\ell}$), magnetic permeability ($\mu_\ell = \mu_0 \mu_{r,\ell}$), thickness ($h_\ell$) for $\ell = 0, 1, \cdots, N$, and $h_0 = h_{N+1} = \infty$, and $\epsilon_0$ and $\mu_0$ are the electrical permittivity and magnetic permeability of vacuum. The infinitely long source parallel to the $y$-axis is located at $(x', z')$ in layer $m$. The wavenumber in layer $\ell$ is $k_\ell^2 = \omega^2 \epsilon_\ell \mu_\ell$, where $\omega = 2\pi f$ and $f$ is the frequency of the electromagnetic waves created by the line source.

The electric field at the observation point $(x, z)$, which can be chosen in any layer, can be determined by evaluating the following Sommerfeld integral:

$$E_y(x, z|x', z') = \frac{1}{4\pi k_\ell} \int_0^\infty \left\{ \tilde{G}(x, z|x', z') \frac{\cos(k_x|x-x'|)}{k_z} \right\} dk_x, \quad (1)$$
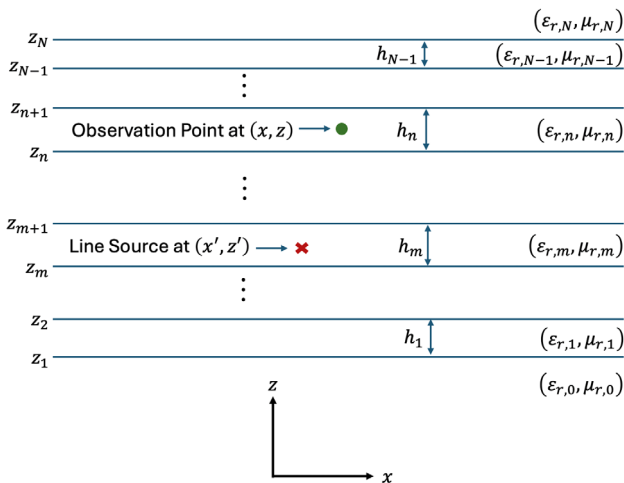


**Fig. 1.** Schematic illustration of a multilayered medium with $N+1$ layers and $N$ interfaces parallel to $x$-axis. The thickness of layer $\ell$ is $h_\ell$. The relative electrical permittivity and magnetic permeability of the material used in layer $\ell$ are $\epsilon_{r,\ell}$ and $\mu_{r,\ell}$, respectively.

where $\tilde{G}(x, z|x', z')$ is the spectral domain LMGF that can be calculated with

$$\tilde{G}(x, z|x', z') = \Phi_\ell e^{u_\ell(z-z_l)} + \Psi_\ell e^{-u_\ell(z-z_{l-1})}, \quad (2)$$

where $\Phi_\ell$ and $\Psi_\ell$ are unknowns that need to be determined according to continuity conditions of the electric and magnetic fields at the interfaces, $k_x$ is the integration variable, $k_{z,\ell}^2 + k_x^2 = k_\ell^2$, and $u_\ell = jk_{z,\ell}$. When the source is in the bottom layer ($m = 0$), then $\Psi_0 = 0$, and similarly, when the source is in the top layer ($m = N+1$), then $\Phi_{N+1} = 0$. By imposing the boundary conditions for electric and magnetic fields, we can create a linear equation to determine all these coefficients, i.e., $\mathbf{AX} = \mathbf{S}$, where $\mathbf{A} \in C^{2N \times 2N}$, $\mathbf{X} \in C^{2N}$, and $\mathbf{X} \in S^{2N}$. The non-zero elements of $\mathbf{A}$ are provided in Appendix A. To construct the vector $\mathbf{X}$, we set

$$\begin{align} x_1 &= \Phi_0, \quad x_{2n} = \Psi_N, \\ x_{2i} &= \Phi_i, \quad x_{2i+1} = \Psi_i, \end{align} \quad (3)$$

for $i = 1, \ldots, N-1$.

To construct the vector $S$, we set

$$\begin{align} S_{2j-1} &= \frac{e^{-u_j|z_{j-1}-z'|}}{u_j}, \quad S_{2j} = \frac{e^{-u_j|z_{j-1}-z'|}}{\epsilon_j}, \\ S_{2j+1} &= -\frac{e^{-u_j|z_j-z'|}}{u_j}, \quad S_{2j+2} = \frac{e^{-u_j|z_j-z'|}}{\epsilon_j}. \end{align} \quad (4)$$

If in Eq. (4), the source is in the bottom layer, i.e., $m = 0$; we then set $S_{2m-1} = 0$ and $S_{2m} = 0$. Similarly, if the source is in the top layer $m = n$, we then set $S_{2m+1} = 0$ and $S_{2m+2} = 0$. After determining the unknown coefficients, we numerically compute Eq. (1) using a 32-point Gauss-Legendre quadrature. It is essential to note that when the source location is fixed and observation points have the same $z$ coordinate but different $x$ values, we must calculate the spectral domain LMGFs only once. Hence, evaluating Eq. (1) for $n_d$ observations on an axis parallel to $\hat{x}$, we calculate all the LMGFs in a single run, reducing the computation time by almost $n_d$ times compared to evaluating them one by one.

## 3. IMPLEMENTATION OF ADJOINT METHOD WITH LMGFs

We start with the following simple example to describe how the adjoint method can be implemented with 2D LMGFs. Assume that we have a 2λ thick substrate between $z = -2\lambda$ and $z = 0$. A line source is at $(x' = 0, z' = -2.5\lambda)$, half wavelength below the substrate. Our goal is to design a substrate that would yield the highest electric field at $(x_t = 0, z_t = 0.5\lambda)$, half wavelength above the substrate. For the sake of simplicity, let us assume that the substrate consists of 10 layers with the same layer thickness ($\lambda/5$), as shown in Fig. 2(a). Assuming all the materials are non-magnetic, we aim to determine each layer's permittivity using the AM.

As explained in [2–9,11], the AM requires only two computations to calculate the gradients with respect to the design parameters. For this problem, we choose our cost function ($\vartheta$) in order to maximize the electric field intensity ($|E|^2$) at the target location $(x_t, z_t)$ and use the following equation to calculate the gradient:

## (a) Step-1

Target Point at $(x_t, z_t)$

$(\epsilon_{r,11} = 1)$

10
9
8
7
6
5
4
3
2
1

$(\epsilon_{r,0} = 1)$

$\lambda/2$

Source at $(x', z')$

$\lambda/2$

## (b) Step-2

$(\epsilon_{r,11} = 1)$

10
9
8
7
6
5
4
3
2
1

$(\epsilon_{r,0} = 1)$

$\lambda/2$

Source at $(x', z')$

## (c) Step-3:

Adjoint Source at $(x_t, z_t)$

$\lambda/2$

$(\epsilon_{r,11} = 1)$

10
9
8
7
6
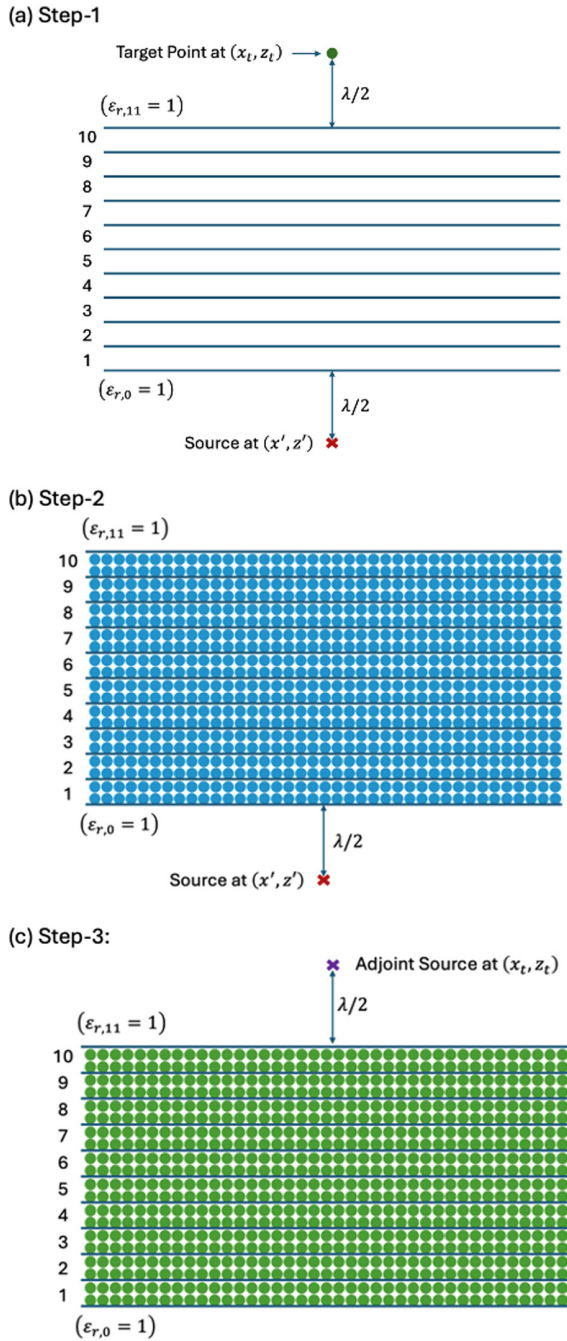5
4
3
2
1

$(\epsilon_{r,0} = 1)$

**Fig. 2.** Schematic illustrations of (a) target, (b) forward, and (c) backward field calculations where small circles and crosses represent field and source points, respectively.

$$\frac{\partial \vartheta}{\partial \epsilon_{r,\ell}} = -2k_0^2 \sum_d \mathrm{Re}\left\{ E_\ell^{\mathrm{forw}} \cdot E_\ell^{\mathrm{adj}} \right\}, \qquad (5)$$

where $E_\ell^{\mathrm{forw}}$ is the electric field created by the original line source and calculated at $d$ observation points located in layer $\ell$ as shown in Fig. 2(b) and $E_\ell^{\mathrm{adj}}$ is the adjoint field calculated at the same observation points due to an adjoint source located at the target position as shown in Fig. 2(c). Analogically, if $E_\ell^{\mathrm{forw}}$ is the value that we obtain with Eq. (1) when there is a line source at $(x', z')$ carrying 1 A of current, then the $E_\ell^{\mathrm{adj}}$ is the value

we obtain from the same equation for a line source at $(x_t, z_t)$ carrying a complex current of $2j E^*(x_t, y_t|x', z')/\omega$ A, where $E^*$ is the complex conjugate of $E$. In other words, our adjoint field at an observation point $(x_d, y_d)$ is

$$E^{\mathrm{adj}} = \frac{2j}{\omega} E^*(x_t, z_t|x', z') E_\ell^{\mathrm{back}}(x_d, z_d|x_t, z_t), \qquad (6)$$

where $E_\ell^{\mathrm{back}}(x_d, z_d|x_t, z_t)$ is the value that we obtain with Eq. (1) when there is a line source at $(x_t, z_t)$ carrying 1 A of current.

Our iterative implementation has five steps that can be formulated as follows.

- Step 1: calculate the electric field $E(x_t, y_t|x', y')$ at the target point where we want to enhance the electric field as shown in Fig. 2(a).
- Step 2: calculate the electric field $E_\ell^{\mathrm{forw}}(x_d, z_d|x', z')$ at observation points that cover a wide range horizontally (e.g., $-4\lambda \leq x \leq 4\lambda$) and dense enough vertically (e.g., 20 observation points per wavelength) inside each layer, as illustrated in Fig. 2(b).
- Step 3: repeat Step 2 by changing the source location with the target location, i.e., calculate $E_\ell^{\mathrm{back}}(x_d, z_d|x_t, z_t)$, as depicted in Fig. 2(c).
- Step 4: update the permittivity of each layer using Eqs. (5) and (7):

$$\epsilon_{r,\ell}^{\mathrm{new}} = \epsilon_{r,\ell}^{\mathrm{current}} + \alpha \frac{\partial \vartheta}{\partial \epsilon_{r,\ell}}, \qquad (7)$$

where $\alpha$ is the learning rate, $\epsilon_{r,\ell}^{\mathrm{current}}$ is the relative electrical permittivity of layer $\ell$ used in the current set of calculations, and $\epsilon_{r,\ell}^{\mathrm{new}}$ is the updated permittivity to be used in the next iteration.

- Step 5: calculate $\sum_\ell |\partial \vartheta / \partial \epsilon_{r,\ell}|$. If it is smaller than the desired threshold value, stop iterating. Otherwise, go back to Step 1.

Note that using symmetry properties of LMGFs [e.g., $E_y(x, z|x', z') = -E_y(-x, z|x', z')$], vectorial evaluation of numerical integration, and parallel computing, the computation time of Steps 2 and 3 can be reduced significantly. Also, if we would like to achieve broadband optimization, then we can update the permittivity of each layer as follows. Let us assume we have $K$ discrete values representing the spectrum of interest where the intensity of the light at wavelength $\zeta$ is $I_\zeta$ for $\zeta = 1, 2, \cdots, K$. Then the permittivity of layer $\ell$ can be computed by

$$\epsilon_{r,\ell}^{\mathrm{new}} = \epsilon_{r,\ell}^{\mathrm{current}} + \frac{\alpha}{K} \sum_{\zeta=1}^{K} I_\zeta \frac{\partial \vartheta_\zeta}{\partial \epsilon_{r,\ell}}. \qquad (8)$$

## 4. NUMERICAL RESULTS

For all the examples presented here, the learning rate ($\alpha$) is set to 0.05.

### A. Permittivity Optimization

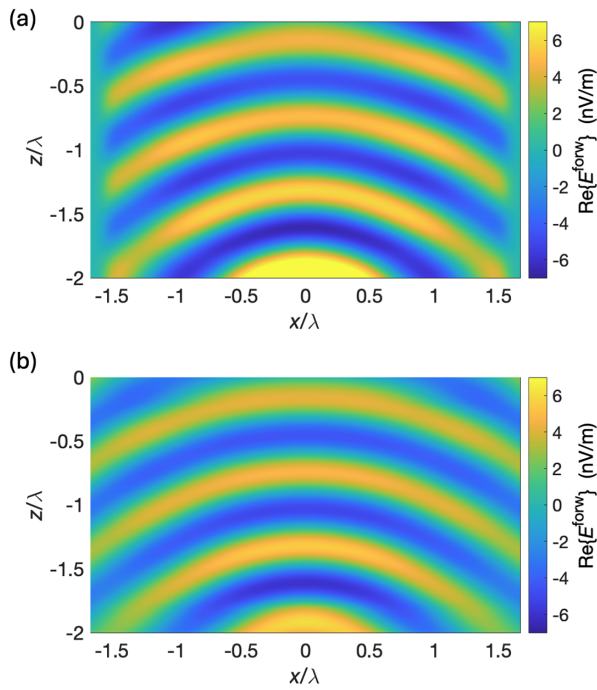We first start with the aforementioned simple optimization problem. Assume the wavelength of the electromagnetic waves

**Fig. 3.** Real part of the electric field ($E^{\text{forw}}$) for the forward calculation obtained using (a) an FDFD solver and (b) LMGFs.
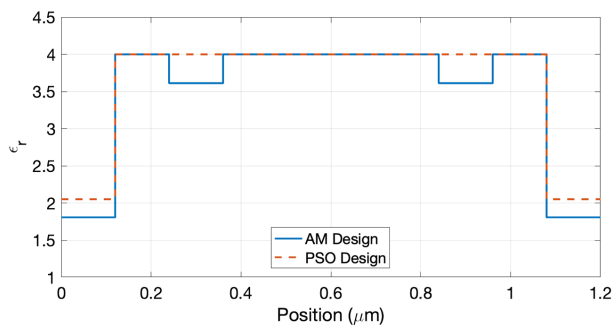


**Fig. 4.** Solid and dashed lines show the optimized permittivity values along the AM- and PSO-designed substrates with 10 thin layers that lead to an 11.09% and an 11.13% enhancement, respectively.

created by the line source is 600 nm, and we are trying to determine the permittivity values of each layer of the substrate, $\epsilon_{r,\ell}$ for $\ell = 1, 2, \cdots, 10$. The top and bottom layers are both air ($\epsilon_{r,0} = \epsilon_{r,11} = 1$). As a design constraint, we enforce $1 \le \epsilon_{r,\ell} \le 4$. For the first iteration of the optimization process, we set $\epsilon_{r,\ell} = 2$ for all $\ell$.

To validate the accuracy of our LMGF implementation, we calculate the electric field values along the substrate using our LMGF formulation and an FDFD solver. For the FDFD solution, we set the unit mesh length to 5 nm. Similarly, for the LMGF implementation, we create a grid in each layer with a grid step length of 5 nm (horizontally and vertically) for $-1\,\mu\text{m} \le x \le 1\,\mu\text{m}$. In Fig. 3, we plot the electric field's real part only for brevity. Due to the perfectly matched layers (PMLs) on both sides of the substrates, the results obtained with the FDFD gradually decrease in those PML regions. Apart from those regions, the results look almost identical.

For the first AM-based substrate optimization example, we assume the same geometry explained at the beginning of the previous section, e.g., the substrate is $2\lambda$ thick from $z = -2\lambda$ to $z = 0$, the line source is at $x' = 0$ and $z' = -2.5\lambda$, and the substrate consists of 10 $\lambda/5$-thick layers. We continue to use 20 points per wavelength sampling density; hence there are 640 target points in each layer, i.e., four points vertically and 160 points horizontally. With the selected design constraint and initial permittivity values, the AM implemented with the LMGF formalism generates a design, as depicted by the blue line in Fig. 4, which yields an 11.1% increase compared to a glass slide with a relative permittivity of 2.25 (corresponding to the refractive index of 1.5), which is the typical value for the permittivity of optical glass substrates. We also implement another numerical optimization method using the PSO method. Using 100 swarms and 300 iterations, the PSO recommends a similar but slightly different design, shown with the red dashed lines in Fig. 4, which yields an 11.13% increase compared to the glass slide. Note that we obtain much more significant enhancements by increasing the maximum electrical permittivity allowed from four to a higher value, e.g., 20. However, since our primary focus is the applicability of the AM method for one-dimensional problems such as substrate optimization using LMGFs, we do not discuss those cases here.

For the second set of substrate optimization studies, we increase the number of layers within the substrate to 240 and follow the same procedure. Since these are $\lambda/120$-thick layers, we have 160 target points in each layer. For the initial step, we set all the relative permittivity values to 2.0 for all 240 thin layers. The PSO implementation uses 2400 swarms, with the maximum number of iterations set to 1000, but the computation ends nearly at the 400th iteration when the cost no longer decreases. The designs recommended by the AM and PSO implementations are plotted in Figs. 5(a) and 5(b). Even though these two designs yield almost the same level of field enhancement, 11.32% and 11.3%, respectively, the designs recommended by these two methods have one very distinct difference. The permittivity profile of the AM design is very smooth, whereas the PSO design has abrupt changes. The reason behind the smooth design of AM is that the permittivity update equation, Eq. (7), is basically an averaging operation that includes the contributions of hundreds of interactions between forward and backward fields. From a practical point of view, the AM design is easier to fabricate, for example, using thin films of acrylonitrile butadiene styrene-based nanocomposites, whose relative permittivity can be tuned to any value between two and seven by changing the ferroelectric barium titanate nanoparticle fill ratio [31]. As pointed out earlier, PSO-like numerical optimization methods face challenges in handling continuous design spaces when the number of parameters to be optimized is large.

In terms of computing time and efficiency, let us make the following comparison. In the PSO implementation, each trial requires only one calculation of Eq. (1). Since we use 2400 swarms and 400 iterations, we compute nearly one million LMGFs. For the AM implementation, we compute 481 sets of LMGFs (240 forward, 240 backward, and one source-to-target), which takes 47 iterations to converge. So, we compute nearly 23,000 LMGFs. Due to this significant difference
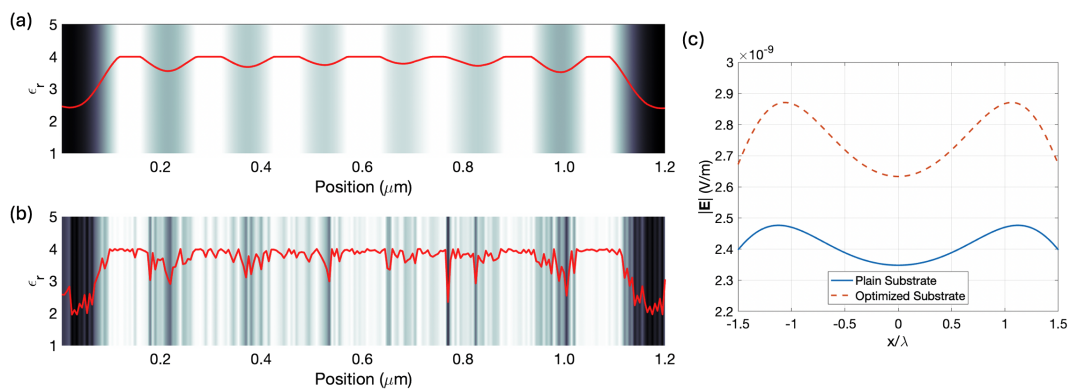
**Fig. 5.** Permittivity values along the (a) AM- and (b) PSO-designed substrates with 240 thin layers that lead to an 11.22% and an 11.2% enhancement, respectively. (c) Electric field intensity values at $z = \lambda/2$ and $-1.5\lambda \leq x \leq 1.5\lambda$, where $\lambda = 600$ nm, assuming a plain substrate with relative permittivity of two (solid curve) and the optimized substrate (dashed curve).

between the number of LMGFs computed in the PSO and AM implementations, the latter requires much less time to achieve the inverse design. We can conclude that the AM not only generates realistic designs with smooth permittivity profiles but also achieves the inverse design more efficiently than PSO-like numerical optimization algorithms due to calculating the gradients based on the laws of physics.

It is well known that both the learning rate and dipole sampling density affect the computation time and efficiency. For our initial studies, the learning rate was set to 0.01, which provided robust but slightly low learning. When we set it to 0.1, we observed oscillations in the cost value rather than a continuous and smooth increase. We chose $\alpha = 0.05$ as the optimum value for the examples presented here to balance this trade-off between accuracy and efficiency. In short, the learning rate in AM optimization problems determines whether we can achieve our goal and, if we can, then how fast we reach our goal. Similarly, when we increase the dipole sampling density from $\lambda/20$ to $\lambda/30$, the computation time for each iteration did not change due to the recursive calculation of LMGFs. However, we did not observe any reduction in the number of iterations during the AM optimization. This verifies that the dipole sampling density of $\lambda/20$ is sufficient to grasp the oscillations in the electromagnetic waves propagating along the multi-layered substrate. Using a higher sampling density is neither necessary nor advantageous. However, when we reduced the dipole sampling density from $\lambda/20$ to $\lambda/10$, the optimization was completed in 161 iterations. The one implemented with $\lambda/5$ sampling density did not even converge. This latter case is probably because a coarser mesh may miss the points where the electric field intensity gets maximized, which leads to sub-optimal or inaccurate design solutions.

Lastly, we would like to discuss the impact of the observation point range on the efficiency and accuracy of the AM implementation. As mentioned before, we calculate the forward and backward electric field values over a $8\lambda$-wide range horizontally. After including the distance between the source and the lower interface of the substrate, we can assume an approximate distance of $5\lambda$ between the source and observation points chosen over the substrate. Again, with a rough calculation, this means that both forward and backward electric field intensities near

the edges of our search domain are one-fifth of the field values calculated along the center, e.g., at $x = 0$. Since the adjoint field calculation includes both terms, the effect over the permittivity update of the dipoles near the edges is roughly 4% of those near the center. As a result, their contribution is limited to the third digit of the final value of the permittivity for each layer. If one is interested in the first two digits only, then a $3\lambda$-wide range would suffice.

## B. Thickness Optimization

In the past two decades, extensive research has focused on monolayers of transition metal dichalcogenides, such as molybdenum disulfide ($MoS_2$) and graphene, commonly called two-dimensional (2D) materials. We utilize $SiO_2$ coated Si substrates with 90 nm or 270 nm thicknesses, illustrated in Fig. 6(a), to work with these 2D materials. These specific thicknesses offer optimal contrast between the coated 2D material and bare regions, facilitating the localization of materials during experiments [32]. Our objective is to design a substrate using the adjoint method to enhance the visibility of 2D materials further. To achieve this objective, we redefine the design question and constraint. Assuming we are limited to two materials, $SiO_2$ and Si, but have the freedom to choose the number, thickness, and order of layers, we seek the optimal design that maximizes contrast for broadband excitation. This optimization problem can be approached in various ways. For instance, one might aim to maximize reflectance from the substrate or power within the 2D material. We adopt the latter approach.

It is essential to note that in this scenario, the source is broadband and far from the substrate, similar to the experiments conducted on 2D-material-based photodetectors. Due to this large distance between the light source and the target, we assume this is a plane-wave-like excitation, not a line source. To define broadband excitation, we assume a bell-shaped spectrum ranging from 400 to 750 nm, with maximum intensity at 575 nm (normalized to one) and relative intensities of 0.4 at 450 and 700 nm. We assume the monolayer $MoS_2$ thickness to be 0.65 nm. The complex electrical permittivity of monolayer $MoS_2$ is determined using a numerical model accounting for the
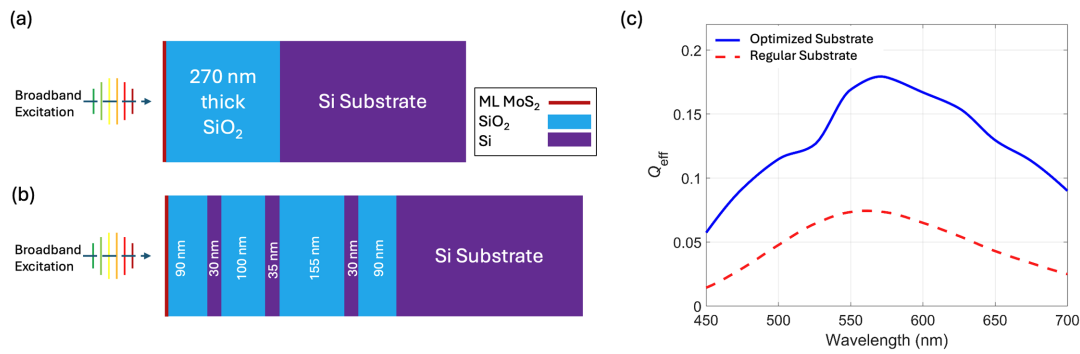
**Fig. 6.** Monolayer MoS$_2$ is placed on top of (a) a simple 270 nm SiO$_2$ coated Si substrate, (b) optimized substrate illuminated with a broadband light source, and (c) quantum efficiency of the MoS$_2$-based phototransistors over regular and optimized substrates assuming gate voltage of 10 V, source-to-drain voltage of 0.5 V, and incidence power of 0.2 μW.

wavelength [33]. Similarly, the electrical permittivity values of Si [34] and SiO$_2$ [35] are calculated as a function of wavelength.

For the AM optimization, we set the number of inner layers (the layers between MoS$_2$ and the Si substrate) to 1000, with each inner layer having a thickness of 1 nm. Initially, the material type of all the inner layers is set to SiO$_2$. Then, during the iterative process, if the $\partial \vartheta / \partial \epsilon_{r,\ell}$ value for layer $\ell$ is larger than the average $\partial \vartheta / \partial \epsilon_r$ calculated over all layers, the material of layer $\ell$ is set to Si. If the value is lower than the average, then the material of layer $\ell$ is set to SiO$_2$. The inverse design is completed in 88 iterations. The final design, which comprises four pairs of SiO$_2$/Si layers with different thicknesses, is shown in Fig. 6(b).

To verify the success of the substrate optimization, we first compute the average power ($E \times H^*$) at the center of the MoS$_2$ film using the FDFD solver for both the current industry standard substrate shown in Fig. 6(a) and the one recommended by the AM method as shown in Fig. 6(b). We achieve to enhance the power absorbed by the MoS$_2$ film across the entire spectrum, with an average enhancement of 72%. Second, we compute the quantum efficiency of the phototransistors made from MoS$_2$ coated SiO$_2$ substrates as follows.

We form a phototransistor by fabricating two metal contacts on opposite sides of a monolayer MoS$_2$ that is placed over a back-gated SiO$_2$/Si substrate. This device can convert optical excitations into electrical currents, and its quantum efficiency is defined as the ratio of the number of generated electrons to the number of incident photons. Briefly, we solve the drift-diffusion equations to calculate the output current of the phototransistors numerically [36]. A detailed description of how the drift-diffusion model is utilized to compute quantum efficiency and other characteristic parameters of 2D material phototransistors can be found in [37]. The quantum efficiencies of the phototransistors made with the regular and optimized substrates are shown in Fig. 6(c). It is observed that for the device with a single layer of SiO$_2$ with a thickness of 270 nm, the quantum efficiency reaches 7.5% at the wavelength around 561 nm. However, with the optimized substrate, the quantum efficiency of 18% is achieved at the wavelength of 571 nm, corresponding to a 141% increase in peak quantum efficiency. The average enhancement across the entire spectrum is 210%.

Similar to this example, we can utilize the AM implemented with LMGFs to design a substrate that maximizes the field at specific wavelengths while minimizing it at others, accommodating different types of excitations, excitation polarizations, and incidence angles. However, implementing the AM method with a full-wave solver would be necessary for more advanced optimization problems, such as if we aim to enhance the fields further based on the surface plasmon resonance of metal nanoparticle arrays fabricated on the substrate.

## 5. CONCLUSION

This study demonstrates the effectiveness of the adjoint method (AM) combined with layered medium Green's functions (LMGFs) for substrate optimization. Through appropriate formulation of the optimization problem and constraints, we harness the unique advantages of AM, which include efficient computation of gradients and suitability for continuous design spaces, to optimize substrate designs aimed at enhancing field properties and transmission characteristics. Our numerical investigations illustrate the proposed methodology's accuracy, efficiency, and versatility, resulting in significant improvements in field intensity for a selected wavelength or wavelength range. Through comparative analysis with particle swarm optimization, we emphasize the superior computational efficiency of AM, highlighting its role as a robust tool for photonics inverse design.

## APPENDIX A

The non-zero elements of **A** are as follows:

$$A_{11} = \frac{1}{u_0}, \ A_{12} = -\frac{e^{-u_1 h_1}}{u_1}, \ A_{13} = -\frac{1}{u_1}, \tag{A1}$$

$$A_{21} = \frac{1}{\epsilon_0}, \ A_{22} = -\frac{e^{-u_1 h_1}}{\epsilon_1} \ A_{23} = \frac{1}{\epsilon_1}, \tag{A2}$$

$$A_{21} = \frac{1}{\epsilon_0}, \ A_{22} = -\frac{e^{-u_1 h_1}}{\epsilon_1}, \ A_{23} = \frac{1}{\epsilon_1}, \tag{A3}$$

$$A_{2N-1,2N-2} = \frac{1}{u_{n-1}}, \ A_{2N-1,2N} = -\frac{1}{u_n}, \ A_{2N-1,2N-1} = \frac{e^{-u_{n-1} h_{n-1}}}{u_{n-1}}, \tag{A4}$$

$$A_{2N,2N-2} = \frac{1}{\epsilon_{n-1}}, \;\; A_{2N,2N} = \frac{1}{\epsilon_n}, \;\; A_{2N,2N-1} = -\frac{e^{-u_{n-1}h_{n-1}}}{\epsilon_{n-1}},$$
$$\text{(A5)}$$

$$A_{2N,2N-2} = \frac{1}{\epsilon_{n-1}}, \;\; A_{2N,2N} = \frac{1}{\epsilon_n}, \;\; A_{2N,2N-1} = -\frac{e^{-u_{n-1}h_{n-1}}}{\epsilon_{n-1}},$$
$$\text{(A6)}$$

$$A_{2i-1,2i-2} = \frac{1}{u_{i-1}}, \;\; A_{2i-1,2i-1} = \frac{e^{-u_{i-1}h_{i-1}}}{u_{i-1}},$$
$$A_{2i-1,2i} = -\frac{e^{-u_i h_i}}{u_i}, \;\; A_{2i-1,2i+1} = -\frac{1}{u_i},$$
$$\text{(A7)}$$

$$A_{2i,2i-2} = \frac{1}{\epsilon_{i-1}}, \;\; A_{2i,2i-1} = -\frac{e^{-u_{i-1}h_{i-1}}}{\epsilon_{i-1}},$$
$$A_{2i,2i} = -\frac{e^{-u_i h_i}}{\epsilon_i}, \;\; A_{2i,2i+1} = \frac{1}{\epsilon_i},$$
$$\text{(A8)}$$

where $i = 2, \ldots, N-1$.

**Disclosures.** The authors declare no conflicts of interest.

**Data availability.** Data underlying the results presented in this paper are not publicly available at this time but may be obtained from the authors upon reasonable request.

## REFERENCES

1. J. S. Jensen and O. Sigmund, "Topology optimization for nano-photonics," Laser Photonics Rev. **5**, 308–321 (2011).
2. C. M. Lalau-Keraly, S. Bhargava, O. D. Miller, *et al.*, "Adjoint shape optimization applied to electromagnetic design," Opt. Express **21**, 21693–21701 (2013).
3. D. Sell, J. Yang, S. Doshay, *et al.*, "Large-angle, multifunctional meta-gratings based on freeform multimode geometries," Nano Lett. **17**, 3752–3757 (2017).
4. S. Molesky, Z. Lin, A. Y. Piggott, *et al.*, "Inverse design in nanophotonics," Nat. Photonics **12**, 659–670 (2018).
5. T. W. Hughes, M. Minkov, I. A. Williamson, *et al.*, "Adjoint method and inverse design for nonlinear nanophotonic devices," ACS Photonics **5**, 4781–4787 (2018).
6. M. H. Tahersima, K. Kojima, T. Koike-Akino, *et al.*, "Deep neural network inverse design of integrated photonic power splitters," Sci. Rep. **9**, 1368 (2019).
7. J. A. Fan, "Freeform metasurface design based on topology optimization," MRS Bull. **45**, 196–201 (2020).
8. M. Minkov, I. A. Williamson, L. C. Andreani, *et al.*, "Inverse design of photonic crystals through automatic differentiation," ACS Photonics **7**, 1729–1741 (2020).
9. J. Jiang, M. Chen, and J. A. Fan, "Deep neural networks for the evaluation and design of photonic devices," Nat. Rev. Mater. **6**, 679–700 (2021).
10. W. Ma, Z. Liu, Z. A. Kudyshev, *et al.*, "Deep learning for the design of photonic structures," Nat. Photonics **15**, 77–90 (2021).
11. A. B. Koucheh, M. A. Kecebas, and K. Sendur, "Adjoint-based optimization of dielectric coatings for refractory metals to achieve broadband spectral reflection," J. Opt. Soc. Am. B **41**, A98–A107 (2024).
12. E. Hassan, B. Scheiner, F. Michler, *et al.*, "Multilayer topology optimization of wideband SIW-to-waveguide transitions," IEEE Trans. Microw. Theory Tech. **68**, 1326–1339 (2020).
13. N. Morrison, S. Pan, and E. Y. Ma, "Physics-agnostic inverse design using transfer matrices," APL Mach. Learn. **2**, 016115 (2024).
14. I. M. Anjum, E. Simsek, S. E. J. Mahabadi, *et al.*, "Use of evolutionary optimization algorithms for the design and analysis of low bias, low phase noise photodetectors," J. Lightwave Technol. **41**, 7285–7291 (2023).
15. C. Forestiere, M. Donelli, G. F. Walsh, *et al.*, "Particle-swarm optimization of broadband nanoplasmonic arrays," Opt. Lett. **35**, 133–135 (2010).
16. B. Saghirzadeh Darki and N. Granpayeh, "Improving the performance of a photonic crystal ring-resonator-based channel drop filter using particle swarm optimization method," Opt. Commun. **283**, 4099–4103 (2010).
17. L. Shen, Z. Ye, and S. He, "Design of two-dimensional photonic crystals with large absolute band gaps using a genetic algorithm," Phys. Rev. B **68**, 035109 (2003).
18. M. Ballarini, F. Frascella, F. Michelotti, *et al.*, "Bloch surface waves-controlled emission of organic dyes grafted on a one-dimensional photonic crystal," Appl. Phys. Lett. **99**, 043302 (2011).
19. K. Toma, E. Descrovi, M. Toma, *et al.*, "Bloch surface wave-enhanced fluorescence biosensor," Biosens. Bioelectron. **43**, 108–114 (2013).
20. R. Badugu, K. Nowaczyk, E. Descrovi, *et al.*, "Radiative decay engineering 6: fluorescence on one-dimensional photonic crystals," Anal. Biochem. **442**, 83–96 (2013).
21. L. Han, D. Zhang, Y. Chen, *et al.*, "Polymer-loaded propagating modes on a one-dimensional photonic crystal," Appl. Phys. Lett. **104**, 061115 (2014).
22. K. Ray, R. Badugu, and J. R. Lakowicz, "Bloch surface wave-coupled emission from quantum dots by ensemble and single molecule spectroscopy," RSC Adv. **5**, 54403–54411 (2015).
23. F. Michelotti, R. Rizzo, A. Sinibaldi, *et al.*, "Design rules for combined label-free and fluorescence Bloch surface wave biosensors," Opt. Lett. **42**, 2798–2801 (2017).
24. M. A. Keçebaş and K. Şendur, "Enhancing the spectral reflectance of refractory metals by multilayer optical thin-film coatings," J. Opt. Soc. Am. B **35**, 1845–1853 (2018).
25. A. Mouttou, F. Lemarchand, C. Koc, *et al.*, "Resonant dielectric multi-layer with controlled absorption for enhanced total internal reflection fluorescence microscopy," Opt. Express **30**, 15365–15375 (2022).
26. A. Mouttou, F. Lemarchand, C. Koc, *et al.*, "Optimization of resonant dielectric multilayer for enhanced fluorescence imaging," Opt. Mater.: X **17**, 100223 (2023).
27. W. C. Chew, *Waves and Fields in Inhomogenous Media* (Wiley, 1999), Vol. **16**.
28. E. Simsek, J. Liu, and Q. H. Liu, "A spectral integral method (SIM) for layered media," IEEE Trans. Antennas Propag. **54**, 1742–1749 (2006).
29. E. Simsek, Q. H. Liu, and B. Wei, "Singularity subtraction for evaluation of green's functions for multilayer media," IEEE Trans. Microw. Theory Tech. **54**, 216–225 (2006).
30. B. Wei, G. Zhang, and Q. Liu, "Recursive algorithm and accurate computation of dyadic Green's functions for stratified uniaxial anisotropic media," Sci. China F **51**, 63–80 (2008).
31. C. Ding, S. Yu, X. Tang, *et al.*, "The design and preparation of high-performance abs-based dielectric composites via introducing core-shell polar polymers64batio3 nanoparticles," Composites Part A **163**, 107214 (2022).
32. E. Simsek and B. Mukherjee, "Visibility of atomically-thin layered materials buried in silicon dioxide," Nanotechnology **26**, 455701 (2015).
33. B. Mukherjee, F. Tseng, D. Gunlycke, *et al.*, "Complex electrical permittivity of the monolayer molybdenum disulfide (MoS$_2$) in near UV and visible," Opt. Mater. Express **5**, 447–455 (2015).
34. D. E. Aspnes and A. Studna, "Dielectric functions and optical parameters of Si, Ge, GaP, GaAs, GaSb, InP, InAs, and InSb from 1.5 to 6.0 eV," Phys. Rev. B **27**, 985 (1983).
35. C. Tan, "Determination of refractive index of silica glass for infrared wavelengths by IR spectroscopy," J. Non-Cryst. Solids **223**, 158–163 (1998).
36. E. Simsek, I. M. Anjum, T. F. Carruthers, *et al.*, "Fast evaluation of RF power spectrum of photodetectors with windowing functions," IEEE Trans. Electron Devices **70**, 3643–3648 (2023).
37. R. Islam, I. M. Anjum, C. R. Menyuk, *et al.*, "Study of an MoS$_2$ phototransistor using a compact numerical method enabling detailed analysis of 2D material phototransistors," Sci. Rep. **14**, 15269 (2024).